Available online at www.sciencedirect.com
ScienceDirect
Trans. Nonferrous Met. Soc. China 32(2022) 2948−2964
Transactions of Nonferrous Metals Society of China
www.tnmsc.cn

Correlation between microstructure and corrosion and cavitation erosion behaviors of nickel aluminum bronze

Qi-ning SONG[1,2], Hui-lin LI[1], Hao-nan ZHANG[1], Hao HONG[1], Nan XU[1], Gen-yuan ZHANG[1], Ye-feng BAO[1], Yan-xin QIAO[3]

1. College of Mechanical and Electrical Engineering, Hohai University, Changzhou 213022, China;
2. Engineering Research Center of Dredging Technology of Ministry of Education, Hohai University, Changzhou 213022, China;
3. College of Materials Science and Engineering, Jiangsu University of Science and Technology, Zhenjiang 212003, China

Received 23 August 2021; accepted 30 December 2021

Abstract: The microstructure, corrosion and cavitation erosion (CE) behaviors of the as-cast and four different heat treated nickel aluminum bronzes (NABs) in 3.5 wt.% NaCl solution were investigated. The results show that after annealing, β' transformed into the eutectoid microstructure, and more κ_{IV} precipitated from α. Less eutectoid microstructure and more β' were obtained after normalizing. The quenched NAB mainly consisted of α and β' phases, and fine, acicular α and κ phases precipitated inside β' after subsequent aging. The largest proportion of the eutectoid microstructure, which underwent severe selective phase corrosion, was responsible for the lowest corrosion resistance of the annealed NAB. The quenched NAB possessed the most protective film and hence the highest corrosion resistance. The mechanical attack was primarily responsible for the CE damage for the as-cast, annealed and normarlized NABs. The quenched and quenched + aged NABs exhibited superior CE resistance because of the high hardness. The CE−corrosion synergy dominantly caused CE degradation, and it was largely attributed to corrosion-enhanced-CE.
Key words: heat treatment; nickel aluminum bronze; corrosion; cavitation erosion; synergistic effect

1 Introduction

Nickel aluminum bronze (NAB) is a typical copper alloy used for manufacturing ship propellers, pumps, valves and pipelines in marine environments. It contains 9−12 wt.% Al, about 6 wt.% each of Fe and Ni, and 1 wt.% Mn [1]. The addition of multiple alloying elements results in the microstructure diversity of NAB. The as-cast NAB consists of α, β' and various κ phases, and these phases have different crystal structures and chemical compositions [2,3]. As a result, galvanic corrosion occurs for the NAB and some phases undergo preferential corrosion. This type of corrosion damage is called "selective phase corrosion (SPC)". The α phase in the eutectoid microstructure and the β' phase suffer severe corrosion in seawater [4−6]. Moreover, some of the NAB components, such as ship propellers, are also subjected to cavitation erosion (CE). CE generally occurs on the hydraulic components due to the variation of the liquid pressure [7]. The cavitation phenomenon generates huge mechanical impact on the surface of hydraulic components, resulting in deformation, mass loss and failure [8−10]. The CE resistance is closely related to the mechanical properties, including strength, hardness, toughness

Corresponding author: Qi-ning SONG, Tel: +86-519-85191938; E-mail: qnsong@hhu.edu.cn;
Yan-xin QIAO, Tel: +86-511-84401184, E-mail: yxqiao@just.edu.cn
DOI: 10.1016/S1003-6326(22)65995-8

and work hardening capacity [10−12]. The phases in the as-cast NAB act differently to the CE impact. It was reported that the α phases experienced plastic deformation initially and they were grievously damaged because of the low hardness. Cracks initiated preferentially at the α/κ interface because of the structure difference, resulting in the detachment of large κ_{II} and collapse of the eutectoid $\alpha+\kappa_{III}$ [8,13]. ZHANG et al [14] found that the cracks were prone to lateral expansion because of the uniformly distributed κ_{IV} in the α matrix, and high density dislocations and deformation twins, which were created in α phases, inhibited the expansion of vertical cracks. Deep cavities were found in the eutectoid $\alpha+\kappa_{III}$ as a result of the occurrence of SPC, and the synergistic effect between corrosion and CE created 31.5% of the total CE mass loss [15].

Many researchers have focused on modifying the microstructures and improving the mechanical properties of the NAB in order to raise the corrosion and CE resistance [16−21]. Friction stir processing [16], laser surface processing (LSP, including laser melting and quenching, etc) [17,19] and hot rolling [21] have been performed on the as-cast NAB. The as-cast microstructure was altered, refined and homogenized as a result of the thermal and mechanical effects during these surface modifying processes. The strength of the as-cast NAB was remarkably improved by FSP without sacrificing the ductility [16]. The hardness was significantly increased by LSP [17,19]. These provided advantages to the CE resistance improvement. Compared with the as-cast substrate, the FSP and LSP NABs also exhibited higher corrosion resistance owing to the occurrence of uniform corrosion and formation of more compact and protective films [17,22]. It can be drawn that the corrosion and CE behaviors are highly related to the microstructure. Thus, clarifying the correlation between microstructure and the corrosion and CE behaviors is essential for the processing parameters (heat input, heating and cooling rates, and post-heat treatment) determination of those modifying methods.

A complex microstructure evolution occurs when the NAB experiences a thermal process, and hence different microstructures can be obtained by performing different heat treatments on the NAB [3,23]. The mechanical properties and corrosion behavior of the heat-treated NABs have already attracted the researchers' attention. KANG et al [24] found that the β' phases were eliminated after annealing at 675 °C, and the plasticity and corrosion resistance increased. The quenched and aged sample exhibited the highest tensile strength, the lowest elongation and the worst corrosion resistance due to the increase of galvanic corrosion sites. The highest fatigue strength was obtained without sacrificing the corrosion resistance by performing normalizing on the as-cast NAB. CHEN et al [25] also reported that quenching, aging and normalizing improved the tensile strength and hardness of the extruded NAB with the decrease of an elongation. The corrosion resistance ranked from worse to better as: aged, quenched, normalized, hot extruded and annealed. However, QIN et al [5] found that quenching and quenching/aging reduced the corrosion rate due to the decrease of the eutectoid $\alpha+\kappa_{III}$, and improved the CE resistance because of the generation of a large number of hard β' phases [5]. It is noted that different corrosion behaviors are reported for NAB after the same heat treatment, because of the differences in the heat treatment parameters (heating rate, temperature and cooling rate) and test methods. Therefore, to establish the relationship between the corrosion and CE behaviors with the specific microstructure is more meaningful and can provide more reliable guidance on the microstructure modifying to achieve the corrosion and CE resistance enhancement of NAB.

In this work, gravimetric and electrochemical measurements were carried out to explore the corrosion behaviors of the as-cast and different heat treated NABs. The CE behaviors were evaluated by performing ultrasonically vibrating CE tests. SEM was applied to observing the corroded and eroded morphologies. The synergistic effects between corrosion and CE were analyzed. The correlation between microstructure and the corrosion and CE behaviors was established.

2 Experimental

2.1 Materials and heat treatments

The investigated base material was a as-cast NAB, and its chemical composition was 9.65 wt.% Al, 5.52 wt.% Fe, 4.57 wt.% Ni, 0.92 wt.% Mn, and balanced Cu. The as-cast NABs were sealed in the

vacuum glass tubes, and four heat treatments were performed using a box-type resistance furnace. The parameters were shown in Table 1. The samples were ground, polished and then etched with a solution of 5 g $FeCl_3$ + 2 mL HCl + 95 mL C_2H_5OH. The microstructures were characterized by an optical microscope. The hardness was measured with a Vickers hardness tester (HV), and at least 15 random points were tested. The testing load was 200 g and the dwelling time was 10 s.

Table 1 Heat treatment methods implemented on as-cast NAB

Sample	Heat treatment
Annealed	(675 °C, 4 h), furnace cooling
Normalized	(830 °C, 2 h), air cooling
Quenched	(1000 °C, 2 h), water cooling
Quenched + aged	((1000 °C, 2 h), water cooling) + ((450 °C, 2 h), water cooling)

2.2 Gravimetric measurements

Specimens with dimensions of 14 mm × 10 mm × 2 mm were prepared for the long-term gravimetric measurements. The samples were ground, cleaned and then immersed in 3.5 wt.% NaCl solution, which was replaced weekly. After different immersion periods, a set of samples were taken out and submerged in a solution of 50 vol.% HCl + 50 vol.% distilled water for 120 s to remove the corrosion products on the surface. The difference between the initial mass before immersion and the final mass with the removal of the corrosion products was equal to the corrosion mass loss. To ensure accuracy, at least five samples were prepared after each immersion period for each NAB.

2.3 Electrochemical measurements

A Gamry Interface1000E potentiostat, along with a typical three-electrode system, was applied to performing the electrochemical measurements. The working electrode was the test sample sealed with epoxy resin with an exposed area of 1 cm^2. A platinum plate and a saturated calomel electrode (SCE) were used as the counter and reference electrodes, respectively. The sample was firstly immersed in 3.5 wt.% NaCl solution for about 1800 s to obtain a stable open circuit potential (OCP), then the electrochemical impedance spectroscopy (EIS) was performed at OCP in a frequency range from 10^5 to 10^{-2} Hz with an oscillation voltage amplitude of 5 mV. Linear polarization (LP) was carried out to obtain the polarization resistance in the range of ±10 mV (vs OCP) at a sweeping rate of 0.125 mV/s. The ZSimpWin 3.21 software was applied to simulating the EIS results. At the end of the immersion duration (30 d), the anodic polarization was conducted at a scanning rate of 0.5 mV/s in the potential range of −0.1 to 0.7 V (vs OCP). The electrochemical tests were repeated at least three times for each NAB. The results were reproducible and represented the average level. Both the gravimetric and electrochemical measurements were performed at room temperature (23−28 °C).

2.4 Cavitation erosion tests

The CE test was carried out according to the ASTM G32—10 standard using an ultrasonically vibrating device [26]. The specimen was placed 0.5 mm just below the ultrasonic probe, and its upper surface was 15 mm deep from the liquid level. The amplitude of the horn was 60 μm, and the vibration frequency was 20 kHz. The duration was 5 h. The temperature of the test solution was maintained at 18−22 °C by circulating cooling water. Each test was conducted at least three times to ensure accuracy.

The electrochemical measurements under CE conditions were realized by connecting the CE device with the potentiostat. The OCP values were recorded under alternating quiescence and CE conditions, with each condition lasting for 1200 s. The polarization curves of the specimens under both the quiescence and CE conditions were recorded from −0.3 (vs OCP) to approximately 0 V (vs SCE) with a scanning rate of 0.5 mV/s. The results were analyzed by the CView 3.2 software. The surface and cross-sectional morphologies of the corroded and eroded specimens were observed by scanning electron microscopy (SEM, JEOL JSM−6360LA).

3 Results and discussion

3.1 Microstructures

Figure 1 exhibits the optical microstructures of the as-cast and heat-treated NABs. The as-cast microstructure is composed of coarse Cu-rich α

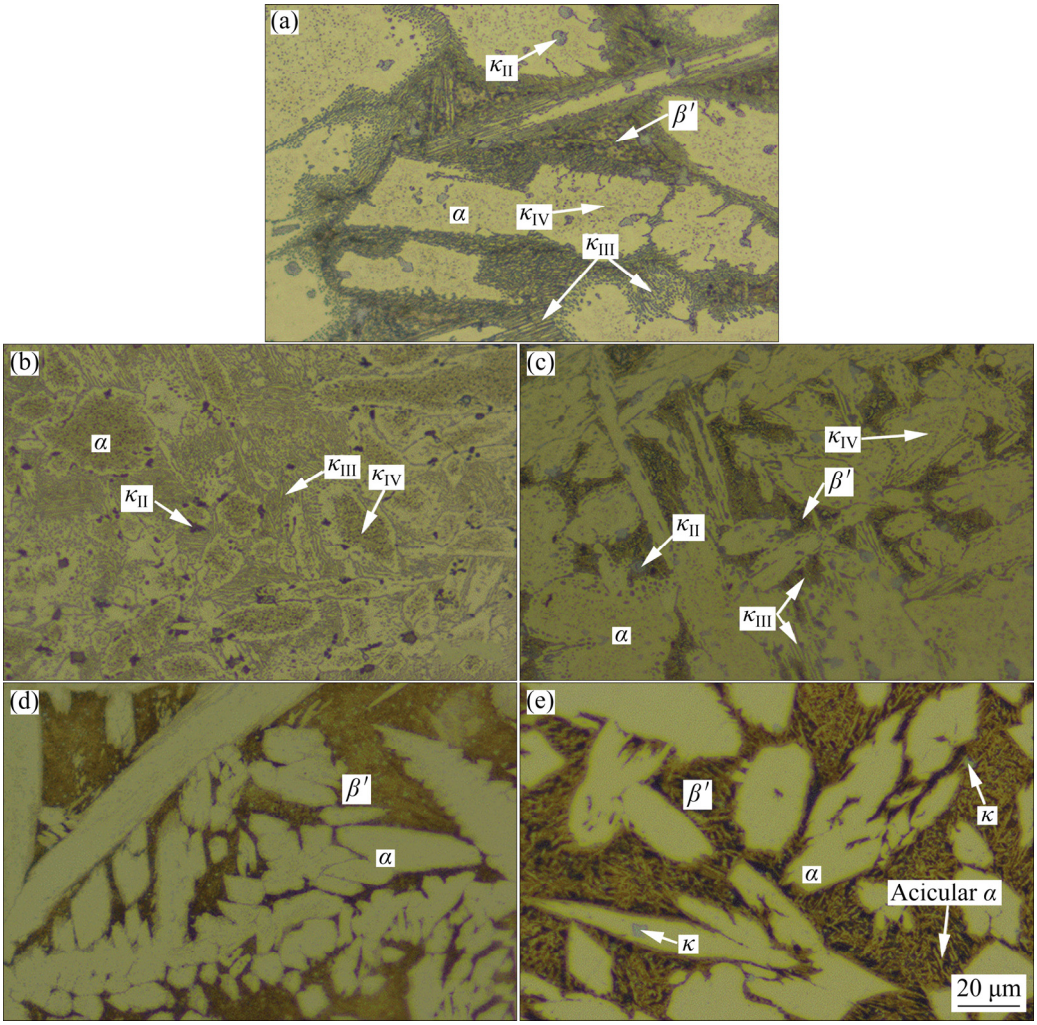

Fig. 1 Optical microstructures of as-cast (a), annealed (b), normalized (c), quenched (d) and quenched + aged (e) NABs

matrix, a small quantity of β' and three types of κ phases, as shown in Fig. 1(a). The κ_{II} phases, which are based on Fe_3Al [2], precipitate at the α/β' boundaries. Some large-sized κ_{II} phases are also found inside the α matrix. The lamellar κ_{III} (based on NiAl [2]) and α phases arrange alternately in the eutectoid microstructure. Fine κ_{IV} phases precipitate inside the α matrix, and they possess similar structure and chemical composition with κ_{II} [2]. It was reported that the NAB possessed a single β phase when heated above 1030 °C. When it was cooled down at a low cooling rate, the κ_{II} phases precipitated from the β phase when the temperature was below 930 °C. The precipitation of Fe-rich κ_{IV} phases inside the α phase occurred below 860 °C. When the temperature dropped below 800 °C, the eutectoid transformation occurred in the rest β phase, and it resulted in the generation of lamellar α and κ_{III}. When the NAB was cooled down at a rapid cooling rate, the high temperature β phase transformed into widmanstatten α, bainite and martensitic β phases. Annealing transformed the β' phases to the eutectoid α+κ_{III}, and promoted the precipitation of κ_{IV} phases in the α matrix. Therefore, the annealed NAB consists of a large number of eutectoid microstructures and κ_{IV} phases, as shown in Fig. 1(b). During normalizing, the as-cast eutectoid α+κ_{III} transformed into β phase when the NAB was heated at 830 °C. However, in the subsequent air cooling process, the precipitation of the eutectoid was restrained because of the relatively high cooling rate. Therefore, the content of β' phases increases and the content of the eutectoid α+κ_{III} decreases in the normalized NAB, as shown in Fig. 1(c). When the as-cast NAB was heated at 1000 °C, the κ phases were dissolved and transformed to the high temperature β phases. During the water cooling process, the precipitation

of κ phases was conspicuously suppressed, and the high temperature β phases transformed to α and β' phases. Therefore, a large number of β' phases and only a small quantity of small-sized κ phases are found in the quenched NAB (Fig. 1(d)). As shown in Fig. 1(e), the growth of κ phases seems to occur during the aging process, and small-sized κ_{II} phases are found inside the α phase of the aged NAB. Moreover, extremely fine acicular α phases and small-sized κ phases are distributed inside the β' phases.

3.2 Corrosion behavior

3.2.1 Gravimetric measurement results

The gravimetric measurement results after immersion in 3.5 wt.% NaCl solution for different time are exhibited in Fig. 2. The mass loss increases with the increase of immersion time for each NAB (Fig. 2(a)), and the longer the immersion time, the lower the mass loss rate (Fig. 2(b)). This phenomenon is attributed to the formation of protective corrosion product films on the NABs, which contributes to the high corrosion resistance of NABs [5,22,27]. After 30 d immersion, the descending order of mass loss rate is: annealed > as-cast > normalized > quenched + aged > quenched. The annealed NAB undergoes the severest corrosion, and the corrosion rate reaches 0.0021 mg/(cm^2·h), which is 1.97 times that of the quenched NAB.

The corroded surface morphologies of the NABs are shown in Fig. 3. The eutectoid microstructures in the as-cast and annealed NABs are preferentially corroded, as shown in Figs. 3(a) and (b), respectively. For the normalized NAB, both the eutectoid microstructures and β' phases suffer preferential corrosion, as presented in Fig. 3(c). The annealed NAB suffers the most grievous corrosion damage, and the grinding scratches induced during sample preparation are indistinct. The quenched and quenched + aged NABs are more lightly and evenly corroded, and preferential corrosion mainly occurs at the β' phases, as shown in Figs. 3(d) and (e), respectively. It is also found that porous corrosion products are discontinuously distributed on the surface. As reported previously, the inner layer of the corrosion product film on NAB mainly contained oxides, and the outer layer mainly consisted of copper hydrochlorides ($Cu_2(OH)_3Cl$ and Cu(OH)Cl) after immersion in 3.5 wt.% NaCl solution [22].

Figure 4 presents cross-sectional morphologies of the NABs after 30 d immersion in 3.5 wt.% NaCl solution. It is found that localized corrosion occurs at the as-cast, annealed and normalized NABs, as shown in Figs. 4(a−c). Deep corrosion pits mainly appear at the eutectoid microstructures of the as-cast and annealed NABs, and at the β' phases of the normalized NAB. The depth of the corrosion pits reaches 6.5, 7.0 and 3.5 μm for the as-cast, annealed and normalized NABs, respectively. In contrast, the corrosion damage is more uniform for the quenched and quenched + aged NABs. Corrosion pits with a maximum depth of 2.3 μm appear on the quenched + aged NAB (Fig. 4(e)), whereas no obvious corrosion pits are found on the quenched NAB (Fig. 4(d)). These results demonstrate that the quenched and the quenched +

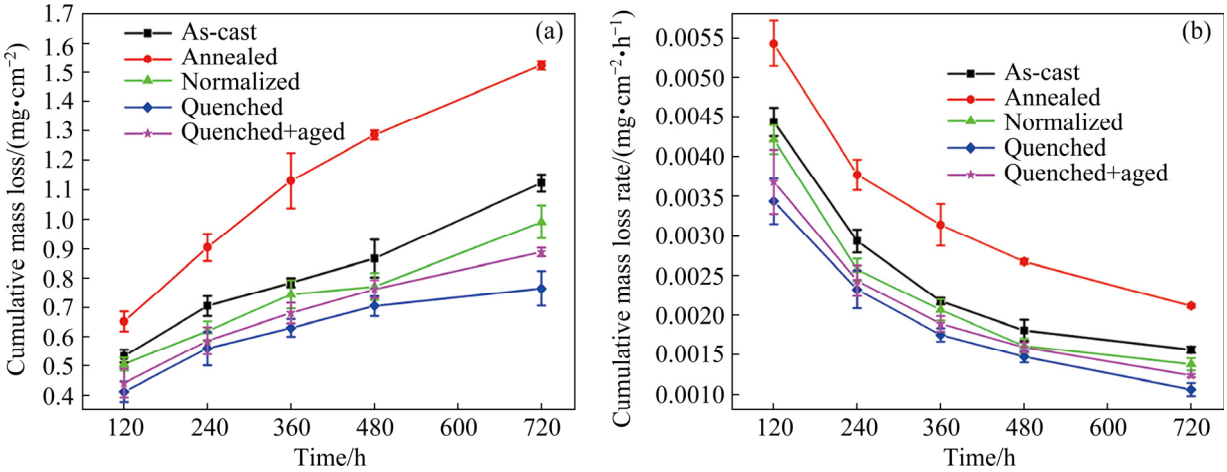

Fig. 2 Mass loss (a) and mass loss rate (b) of different NABs after immersion in 3.5 wt.% NaCl solution for 30 d

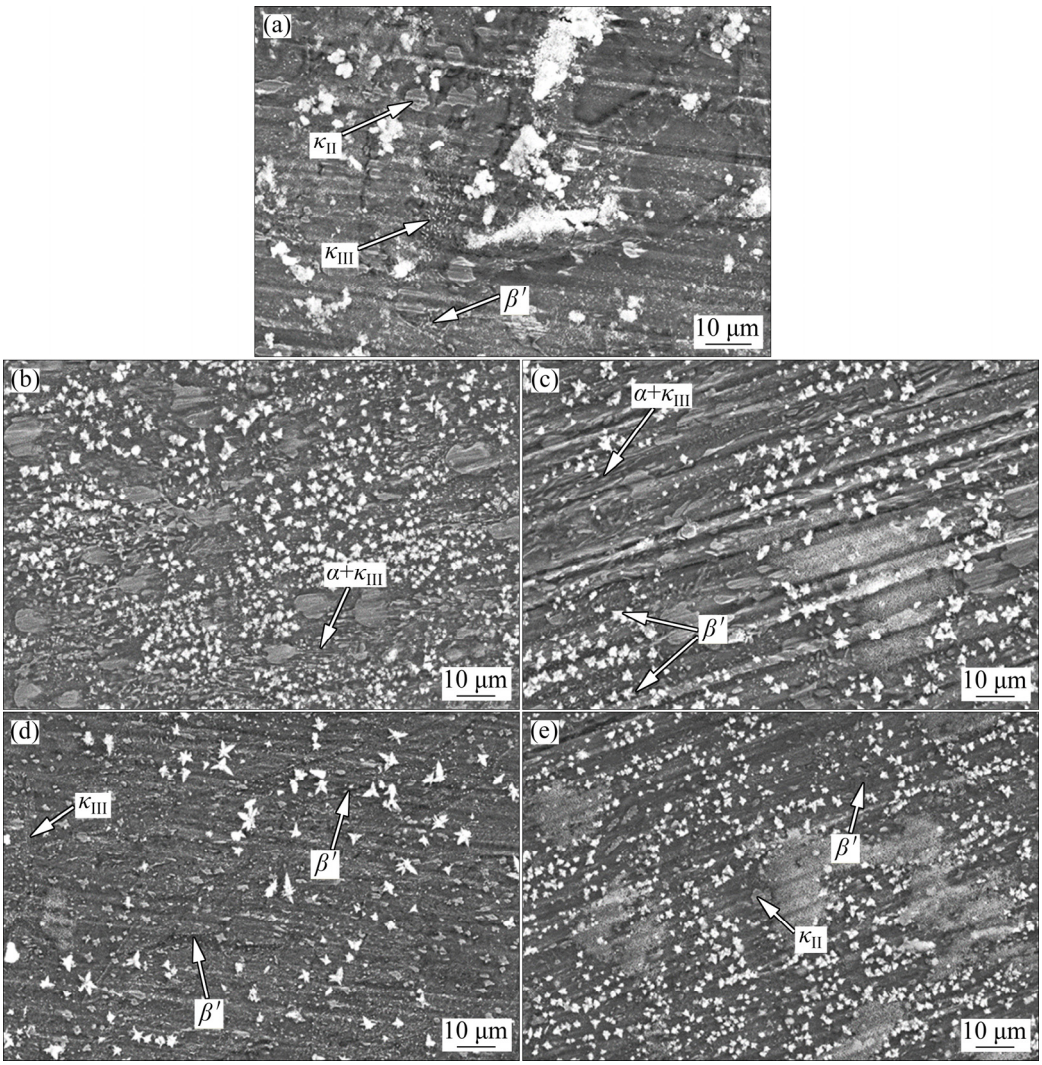

Fig. 3 Surface morphologies of different NABs after immersion in 3.5 wt.% NaCl solution for 30 d: (a) As-cast; (b) Annealed; (c) Normalized; (d) Quenched; (e) Quenched + aged

aged NABs exhibit higher corrosion resistance than other three NABs, coinciding with the gravimetric measurement results.

Inside the eutectoid microstructure of the as-cast NAB, the lamellar α and κ_{III} phases have different structures and chemical compositions [2,3]. When immersed in seawater, the NiAl-based κ_{III} acts as the cathode and it is slightly corroded owing to the quick formation of an Al_2O_3 film. The Cu-rich α phase acts as the anode and suffers preferential corrosion [4,28]. Many tiny precipitates are also found inside the β' phases [2,29], and galvanic corrosion is also generated between these precipitates and the β' matrix. Therefore, the β' phase exhibits poor corrosion resistance to seawater [4−6,29]. The annealed NAB shows lower corrosion resistance than the as-cast NAB, because it possesses a larger quantity of eutectoid microstructures. Even though the normalized NAB contains a high number of β' phases, it exhibits higher corrosion resistance than the as-cast NAB, probably because the galvanic corrosion at the lamellar α and κ_{III} with continuous and alternately-arranged structures in the as-cast NAB is more grievous [4]. Thus, the decrease of the eutectoid microstructures contributes to the relatively high corrosion resistance of the normalized NAB.

For the quenched NAB, the precipitation of eutectoid microstructures is suppressed because of the rapid cooling rate. The Fe, Ni and Al atoms are largely reserved in the β' and α phases instead of being consumed by precipitating κ phases. This promotes the formation of a more homogeneous and protective film on the surface. Moreover, the

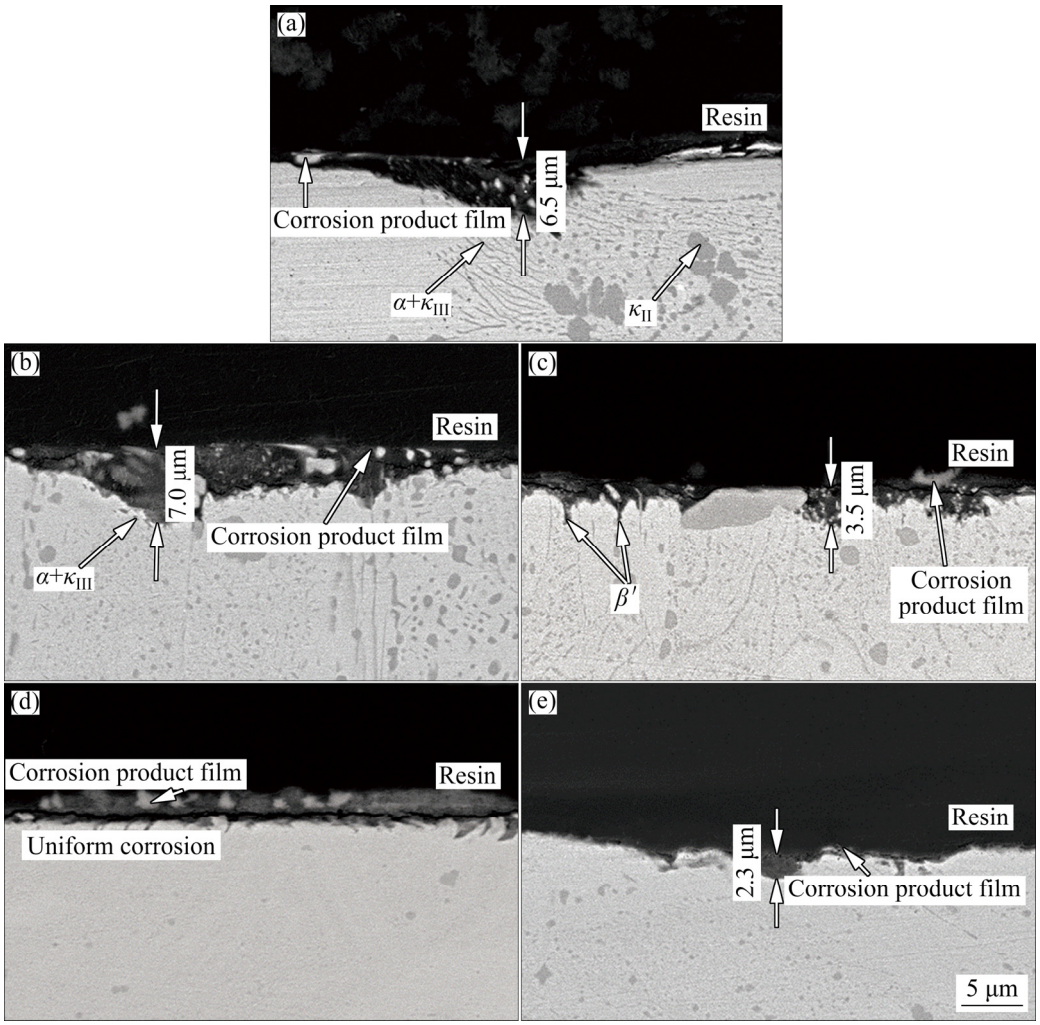

Fig. 4 Cross-sectional morphologies of different NABs after immersion in 3.5 wt.% NaCl solution for 30 d: (a) As-cast; (b) Annealed; (c) Normalized; (d) Quenched; (e) Quenched + aged

corrosion potential difference between the β' and α phases is small since these two phases are both Cu-based solid solution. Therefore, the quenched NAB presents superior corrosion resistance. Similar results were also reported by QIN et al [5]. For the quenched + aged NAB, fine α and κ phases are precipitated from the β' phase. This increases the number of galvanic corrosion sites and raises the corrosion rate. As a consequence, the quenched + aged NAB shows poorer corrosion resistance than the quenched one.

3.2.2 Electrochemical properties

The EIS results of the as-cast and heat-treated NABs after different exposure periods to 3.5 wt.% NaCl solution are presented in Fig. 5. Generally, the capacitive reactance arc in the low frequency region of the Nyquist plots corresponds to the charge transfer and film formation processes on the surface. The larger the semi-diameter of the capacitive reactance arc is, the better the corrosion resistance is [30−33]. With extending the exposure time, the semi-diameter of the capacitive reactance arc and the modulus value ($|Z|$) in the low frequency region increase, indicating the improvement of the corrosion resistance and the formation of protective films. The film on the quenched NAB grows the most rapidly and exhibits the highest protectiveness, followed by the quenched + aged, normalized, as-cast and annealed NABs.

The equivalent circuit model used to fit the EIS results is shown in Fig. 6. As previously reported, the film on the NAB surface contained oxides (Cu_2O and Al_2O_3) in the inner layer, and hydrochlorides (Cu(OH)Cl or $Cu_2(OH)_3Cl$) in the outer layer [22]. Therefore, R_{fout} and R_{fin} are used to represent the film resistances of the porous outer

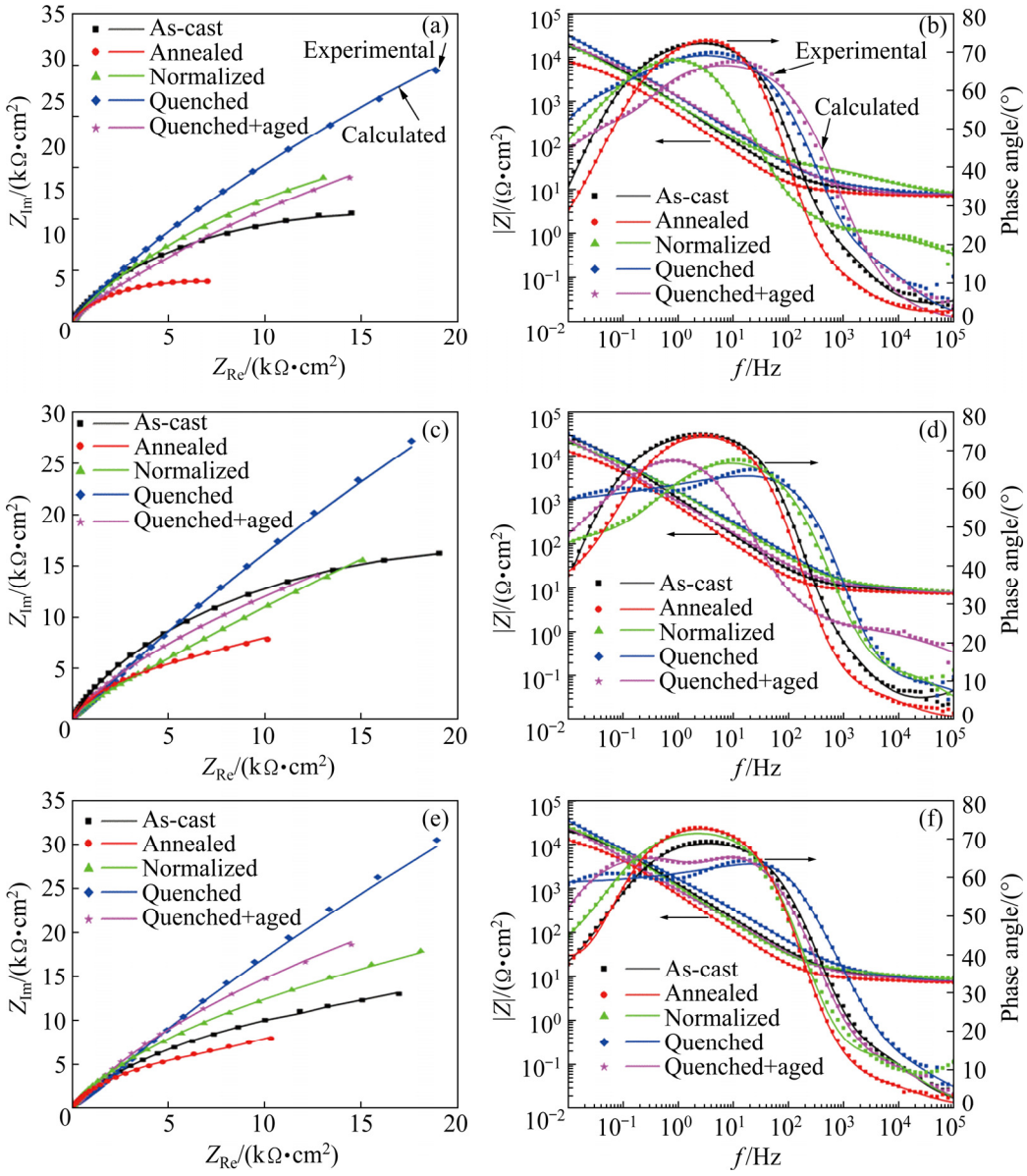

Fig. 5 Nyquist (a, c, e) and Bode (b, d, f) curves of different NABs after immersion in 3.5 wt.% NaCl solution for different time: (a, b) 10 d; (c, d) 20 d; (e, f) 30 d

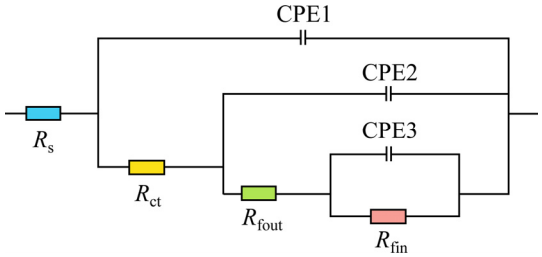

Fig. 6 Equivalent circuit model used for fitting EIS results of different NABs after immersion in 3.5 wt.% NaCl solution

layer and compact inner layer, respectively. R_{ct} is the charge transfer resistance and R_s is the resistance of the solution. The "diffusion effect" caused by the surface roughness or inhomogeneity on the electrode is also taken into consideration, thus constant phase angle elements (CPE) are used and can be quantified as follows [32,34]:

$$Z_{CPE}=[C(j\omega)^n]^{-1} \quad (1)$$

where Z_{CPE} is the impedance of the CPE, C is the capacitance, j is the imaginary number, ω is the angular frequency, and n is the dimensionless exponent. CPE is an ideal capacitor when n=1.

The fitting results are shown in Fig. 5. Relevant electrochemical parameters of three representative NABs are listed in Table 2. The small value of $\sum\chi^2$ (χ^2 is the Chi-square value) testifies

that the selected equivalent circuit can well fit the EIS results. The R_{fout}, R_{fin} and R_{ct} increase for all the NABs as the immersion time extends, indicating the increase of the film protectiveness and the charge transfer resistance. The R_{fout} is much lower than the R_{fin}, demonstrating that the film protectiveness is highly determined by the inner oxide film. Moreover, the value of capacitance C_3 is much lower than that of C_2, and this also proves the compactness and high protectiveness of the inner film. The quenched NAB has the largest R_{ct} and R_{fin}, and hence the highest corrosion resistance.

The linear polarization resistance results after immersion in 3.5 wt.% NaCl solution for different time are illustrated in Fig. 7(a). It can be seen that the R_p increases initially and then tends to reach constant with increasing the immersion time for all the NABs. After the same immersion periods, the descending order of R_p is: quenched > quenched + aged > normalized > as-cast > annealed. The larger the R_p, the higher the corrosion resistance and the smaller the corrosion rate [30]. This result also verifies the formation of protective corrosion product films, and it is consistent with the above EIS and gravimetric measurement results. Figure 7(b) shows the anodic polarization curves of the NABs, which were immersed for 30 d in 3.5 wt.% NaCl solution (noted as the filmed NABs hereinafter). The polarization curves of the unfilmed NABs (initial condition) are also presented in Fig. 7(c) for comparison. It is found that all the NABs exhibit similar electrochemical corrosion behaviors in the initial stage. Heat treatment hardly changes the electrochemical process since the chemical composition of the as-cast NAB is not altered. The active dissolution of copper and the formation of copper oxides occurred in the anodic process [35,36]. The Tafel slope β_a (fitted using CView software, not shown) is close to 60 mV/dec for each NAB, and this corresponds to

Table 2 Fitting data of EIS results for different NABs using equivalent circuit presented in Fig. 6

Parameter	As-cast			Normalized			Quenched		
	10 d	20 d	30 d	10 d	20 d	30 d	10 d	20 d	30 d
$R_s/(\Omega\cdot cm^2)$	7.143	6.57	8.233	6.417	7.12	7.48	6.543	7.512	8.001
$R_{ct}/(k\Omega\cdot cm^2)$	7.314	14.714	40.28	9.110	15.68	55.17	12.34	26.13	90.23
$C_1/(\mu F\cdot cm^{-2})$	307.1	213.1	179.2	352	247.2	198.8	413.1	304.2	237.9
n_1	0.713	0.625	0.578	0.832	0.837	0.643	0.777	0.714	0.623
$R_{fout}/(k\Omega\cdot cm^2)$	0.414	1.001	2.026	0.301	0.942	1.41	0.209	0.896	0.903
$C_2/(\mu F\cdot cm^{-2})$	181.9	300.2	599	299.3	578.2	1000.3	482.9	992.7	1824.1
n_2	0.699	0.832	0.715	0.887	0.713	0.764	0.812	0.836	0.655
$R_{fin}/(k\Omega\cdot cm^2)$	2.98	8.735	16.24	4.77	10.585	26.73	9.142	22.33	39.996
$C_3/(\mu F\cdot cm^{-2})$	3.427	1.873	1.32	25.17	9.24	15.42	110.3	70.62	41.7
n_3	0.595	0.718	0.891	0.729	0.822	0.606	0.691	0.702	0.881
$\sum\chi^2/10^{-4}$	0.88	2.60	3.98	10.32	2.99	3.87	15.83	5.53	2.06

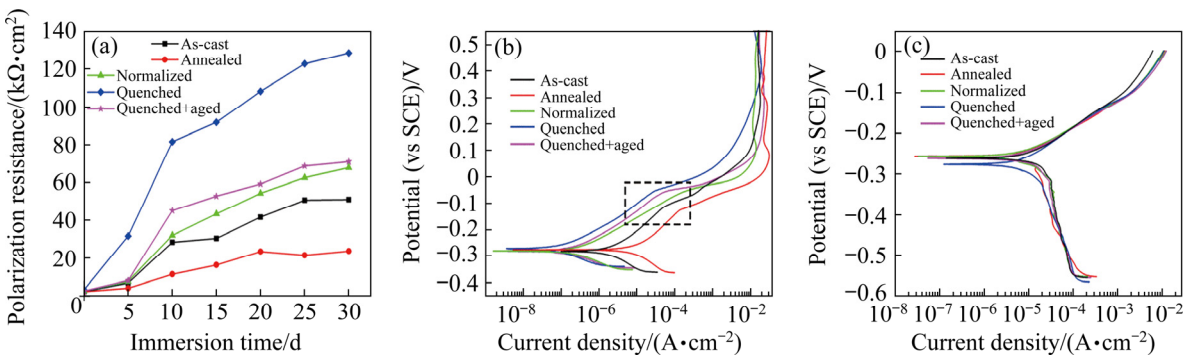

Fig. 7 Linear polarization resistance as function of immersion time (a), anodic polarization curves after 30 d immersion (b) and polarization curves of fresh (quiescent) samples (c) for NABs in 3.5 wt.% NaCl solution

the formation of cuprous products (CuCl) in the anodic process for different NABs [36,37]. Oxygen reduction is the primary cathodic reaction [38,39]. As also reported previously, the friction stir processed and laser surface melted NABs also exhibited similar electrochemical corrosion behaviors with the as-cast NAB in spite of the microstructure change [13,40]. It seems that the filmed NABs exhibit a passive behavior when the applied potential is lower than 0 V (vs SCE) (dashed box in Fig. 7(b)), and the current density increases slightly as the potential increases. The annealed NAB possesses the highest passivation current density among the five samples.

3.3 CE behavior

3.3.1 CE mass loss results

The CE mass loss results of different NABs are presented in Fig. 8. At the end of the CE duration (5 h), the mass loss from high to low ranges as: annealed > as-cast > normalized > quenched > quenched + aged in both distilled water and 3.5 wt.% NaCl solution (Figs. 8(a) and (b)). As presented in Figs. 8(c) and (d), the CE mass loss rate increases dramatically with the increase of the CE time in both solutions for the as-cast, annealed and normalized NABs. In contrast, the mass loss rate is lower and slightly increases with the increase of the CE time for the quenched and quenched + aged NABs. The CE mass loss rate of the annealed NAB in 3.5 wt.% NaCl solution reaches 1.0583 mg/(cm^2·h), which is 1.15 times larger than that of the quenched + aged NAB. In addition, it can be seen that the total mass loss in 3.5 wt.% NaCl solution is higher than that in distilled water for all NABs. The mass loss rate in 3.5 wt.% NaCl solution increases by 31% for the annealed NAB and 195% for the quenched NAB, compared with the results in distilled water after a CE period of 5 h.

In distilled water, the NABs are mechanically attacked and the CE resistance depends on the surface microstructure and mechanical properties. Table 3 presents the hardness results of different NABs. The quenched NAB contains a large number of β' phases, which have high hardness. The

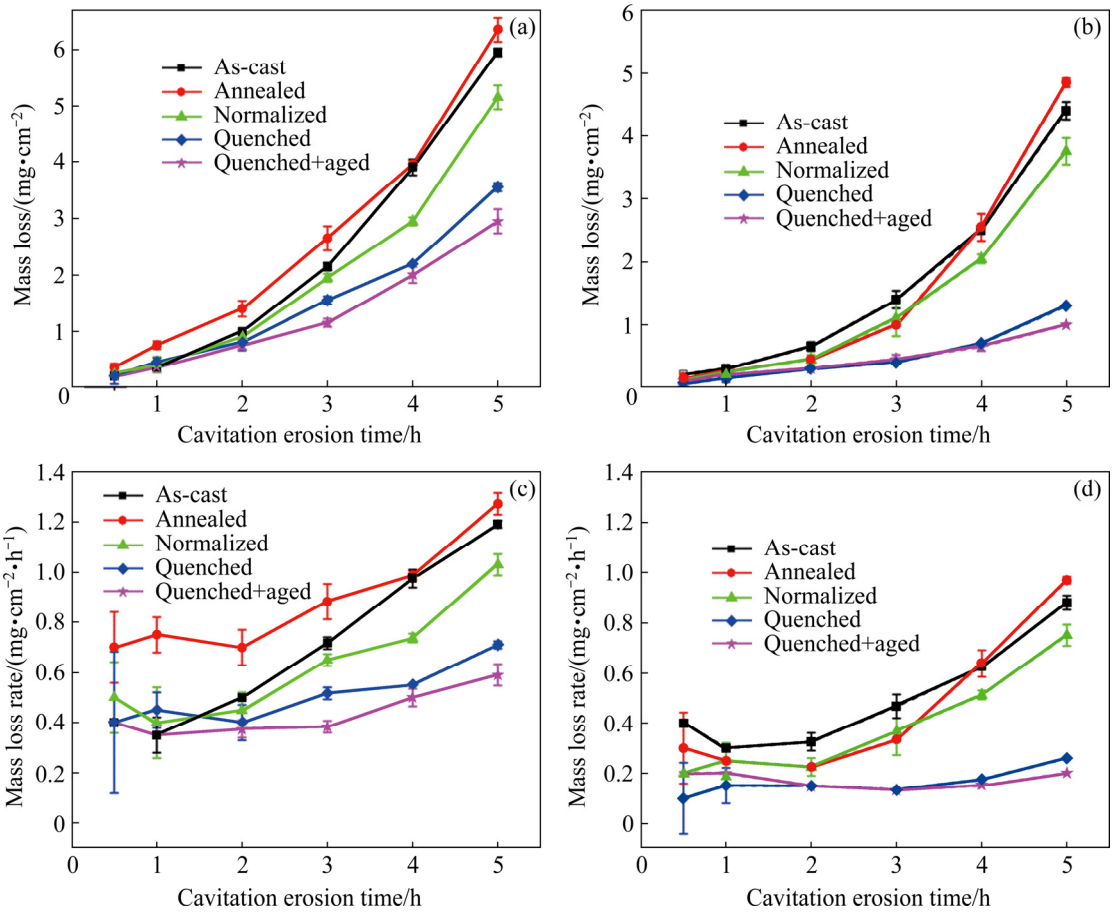

Fig. 8 Mass loss (a, b) and mass loss rate (c, d) of different NABs after CE for different periods in 3.5 wt.% NaCl solution (a, c) and distilled water (b, d)

hardness of the α phases is also raised because more alloying elements (Fe, Ni and Al) are reserved in the α phases, rather than precipitated as κ phases. After subsequent aging, the precipitation of fine κ phases inside α and β' phases causes further hardness improvement. In contrast, the annealed, normalized and as-cast NABs contain a much larger proportion of soft α matrix, and the eutectoid microstructure also exhibits a lower hardness than the β' phase. Therefore, the quenched and the quenched + aged NABs have a much higher hardness and lower CE mass loss rate than the other three NABs.

However, in 3.5 wt.% NaCl solution, the NABs are simultaneously damaged by the mechanical erosion and electrochemical corrosion. A positive synergy exists between these two effects, and it results in additional mass loss [15,41,42]. Based on the corrosion behavior results stated above, all the NABs undergo SPC, which increases the surface roughness, deteriorates the mechanical performance and consequently accelerates the CE damage.

Figures 9 and 10 present the eroded surface and cross-section morphologies of different NABs after a CE period of 5 h in 3.5 wt.% NaCl solution,

Table 3 Vickers hardness results of various phases for different NABs

Phase	As-cast	Annealed	Normalized	Quenched	Quenched + aged
α	165±16	182±5	179±2	220±25	217±18
$\alpha+\kappa_{III}$	188±18	198±11	−	−	−
β'	−	−	184±10	282±18	290±15

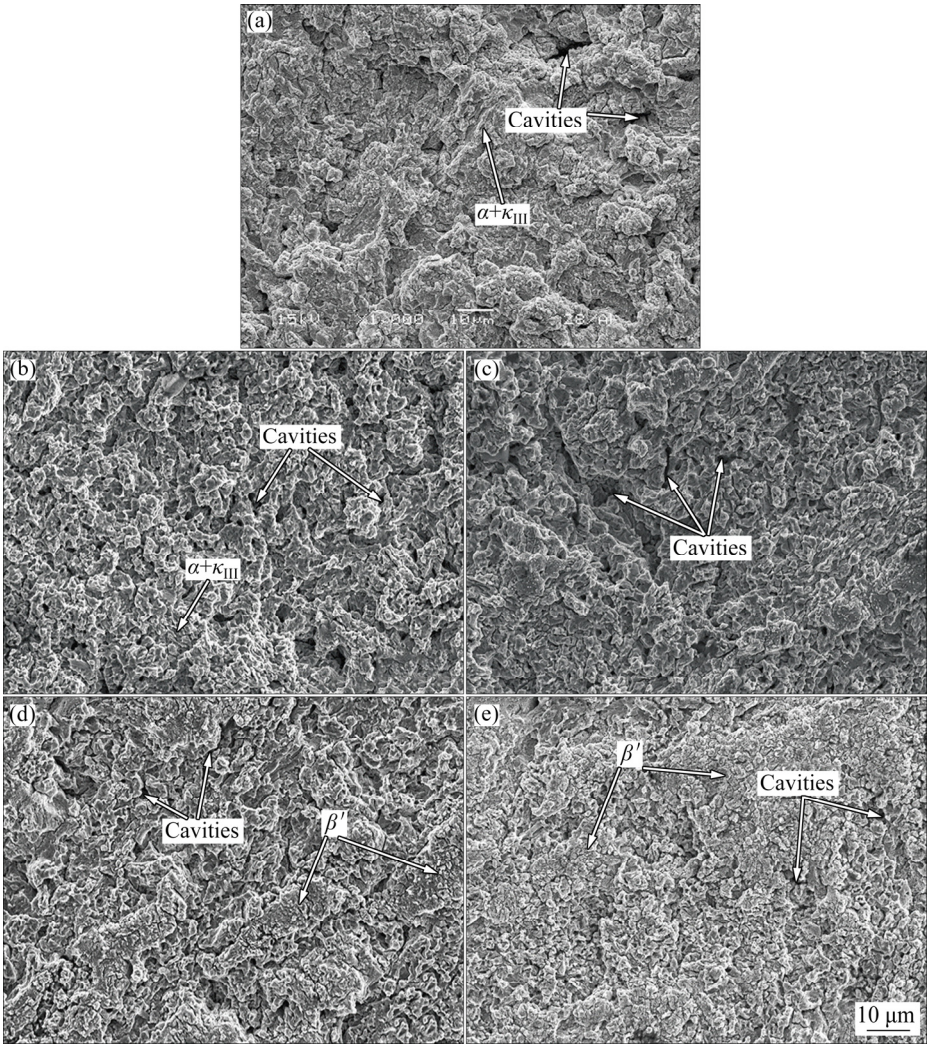

Fig. 9 Surface morphologies of different NABs after CE in 3.5 wt.% NaCl solution for 5 h: (a) As-cast; (b) Annealed; (c) Normalized; (d) Quenched; (e) Quenched + aged

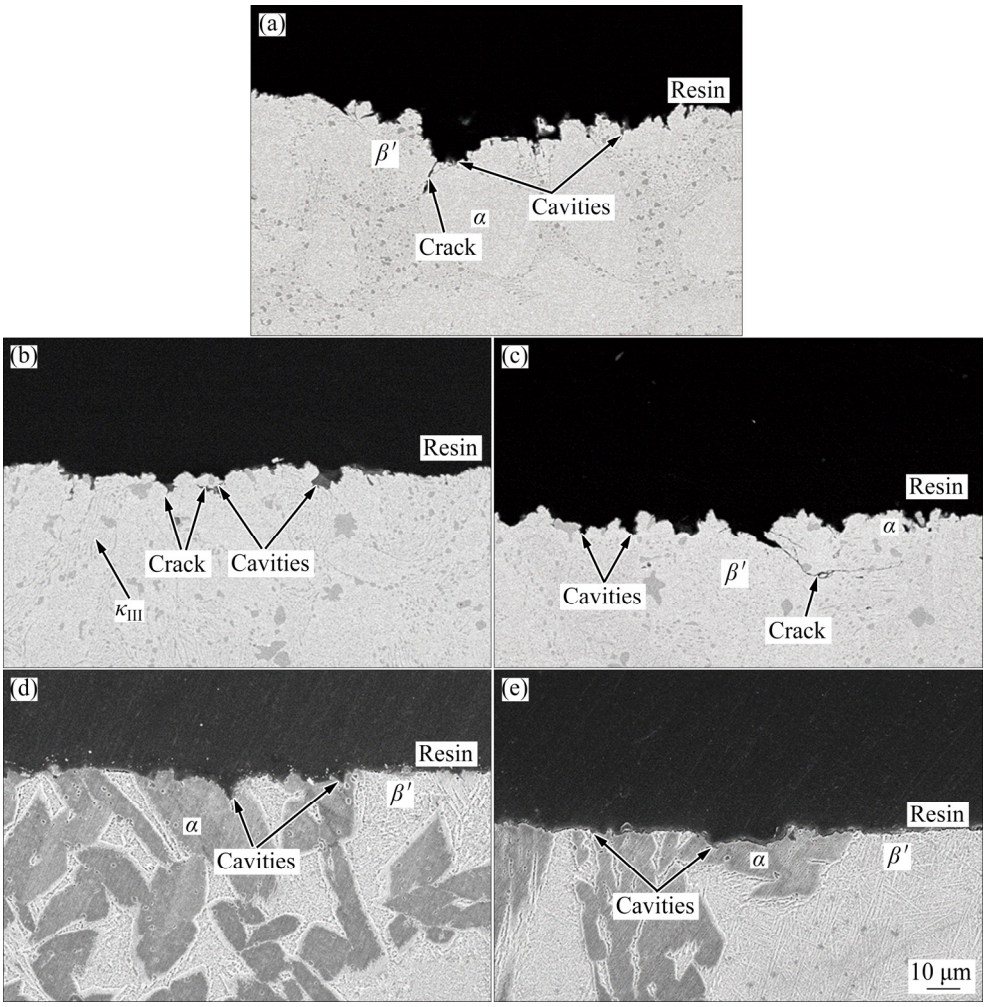

Fig. 10 Cross-sectional morphologies of different NABs after CE in 3.5 wt.% NaCl solution for 5 h: (a) As-cast; (b) Annealed; (c) Normalized; (d) Quenched; (e) Quenched + aged

respectively. For the as-cast, annealed and normalized NABs, deep cavities spread all over the surface, as presented in Figs. 9(a−c). The soft α matrix is severely damaged. The debris of the eutectoid α+κ_{III} with high hardness is found on the surfaces of the as-cast and annealed NABs. However, severe corrosion occurs at the eutectoid microstructure and aggravates the CE damage. As shown in Figs. 10(a) and (b), large cavities appear as a result of the collapse of the eutectoid microstructure. Moreover, long cracks are found at the bottom of the cavities and propagate perpendicularly (Fig. 10(a)). For the normalized NAB, cavities and cracks are also found at the β' phases, which possess inferior corrosion resistance, as shown in Fig. 10(c). The eroded surface is relatively flat for the quenched and quenched + aged NABs, and no deep cavities are found on the surface, as shown in Figs. 9(d) and (e). The β' phases with higher hardness are reserved on the surface, but they undergo preferential corrosion, as discussed above. The cavities are mainly found at the soft α phases, as shown in Figs. 10(d) and (e).

3.3.2 Electrochemical behavior under CE condition

Figure 11 shows the OCP results of the as-cast and heat-treated NABs under the condition of alternate 20 min quiescence and 20 min CE. For all the NABs, CE shifts the OCP in the negative direction. Once CE stops, the OCP increases again and reaches the value close to that under the quiescence condition. In a chloride-containing solution, a protective film containing Cu_2O and Al_2O_3 forms on the surface of NAB [27]. However, the film is destructed by CE and the anodic process is significantly accelerated, resulting in the decrease of OCP [43,44]. ZHANG et al [45] also reported that decrease of the OCP was caused by sliding erosion [45]. When CE stops, the OCP rises

because a new film can be rapidly built on the NAB surface, owing to the high affinity between Al and O [28]. It is noted that CE causes the largest OCP drop of approximately 40 mV for the annealed NAB, whereas the OCP drop is smaller for the quenched and quenched +aged NABs. This result demonstrates that the films on the quenched and quenched + aged NABs are probably more resistant to the mechanical CE attack and can be repaired easily.

Figure 12 shows the polarization curves of the as-cast and heat-treated NABs under the CE condition in 3.5 wt.% NaCl solution. The electrochemical parameters under both the quiescence (results shown in Fig. 7(c)) and CE conditions are listed in Table 4. It can be seen that CE increases the corrosion current density by nearly an order of magnitude for all the NABs, compared with the results under the quiescence condition. CE

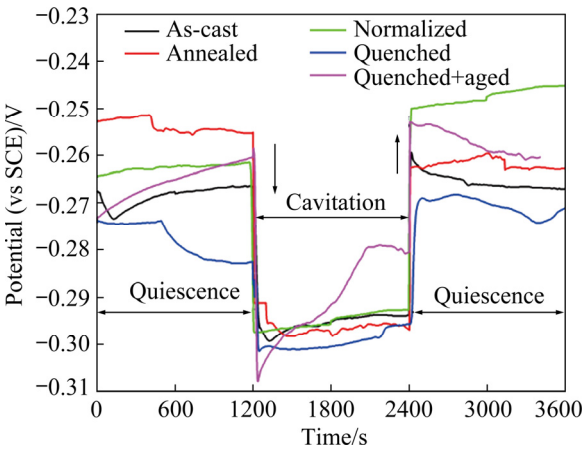

Fig. 11 OCP results of different NABs under condition of alternate 20 min quiescence and 20 min CE

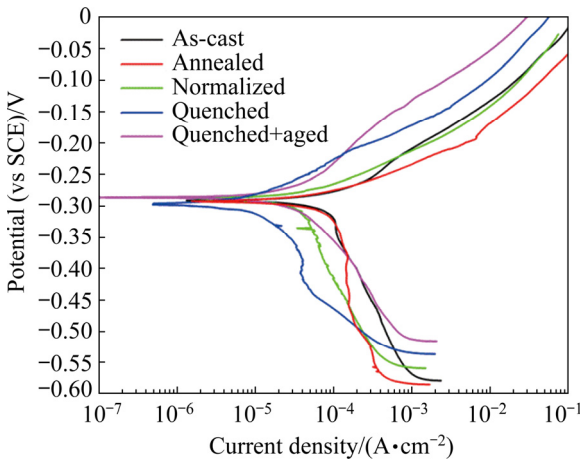

Fig. 12 Potentiodynamic polarization curves of different NABs under CE condition in 3.5 wt.% NaCl solution

destroys the film and makes the fresh substrate exposed to the corrosive medium, resulting in accelerated corrosion rate [6,15]. The quenched and quenched + aged NABs exhibit smaller J_{corr} and larger R_p, indicating that they possess higher corrosion resistance even under the CE condition.

3.4 Synergistic effect between corrosion and CE

As mentioned above, the CE damage (T) is caused by cumulative effect of different components, namely the pure CE (E), pure corrosion (C) and the CE-corrosion synergy (S) in a corrosive medium. S is induced by two factors, namely the corrosion-enhanced-CE (ΔE) and CE-enhanced-corrosion (ΔC). The relationship can be expressed by the following formula [46]:

$$T=E+\Delta E+C+\Delta C=E+C+S \quad (2)$$

In the present study, T and E are quantified using the CE mass loss rates in 3.5 wt.% NaCl solution and distilled water, respectively. C corresponds to the corrosion rate in quiescent 3.5 wt.% NaCl solution. The calculation procedure of ΔE and ΔC was stated in our previous study [15]. The mass losses caused by different components are listed in Table 5.

The contribution of each component to the total mass loss is illustrated in Fig. 13. The C/T value is the smallest for each NAB. The E/T value is the largest for the as-cast, annealed and normalized NABs, indicating that the pure mechanical attack is primarily responsible for the CE damage. The CE-corrosion synergy also plays a crucial role in the CE process and the S/T value is up to approximately 25%. The $\Delta E/T$ and $\Delta C/T$ are fairly close. Corrosion decreases the cohesion of phase boundaries and mechanical properties, and thus results in accelerated CE damage. As indicated in Table 3, these three NABs have relatively low hardness, and CE easily creates large surface roughness, deep cavities and long cracks as a result. This leads to the increase of exposed area to the corrosive medium and the number of active dissolution sites. Therefore, the CE-enhanced-corrosion is as considerable as the corrosion-enhanced-CE.

For the quenched and quenched + aged NABs, the S/T value reaches 62.17% and 64.61%, respectively. This result demonstrates that the CE-corrosion synergy is the dominant factor that

Table 4 Electrochemical parameters of different NABs in 3.5 wt.% NaCl solution under quiescence and CE conditions

Sample	Quiescence			CE		
	φ_{corr}(vs SCE)/V	J_{corr}/(A·cm^{-2})	R_p/(kΩ·cm^2)	φ_{corr}(vs SCE)/V	J_{corr}/(A·cm^{-2})	R_p/(kΩ·cm^2)
As-cast	−0.259	7.0427×10^{-6}	2.281	−0.295	9.8500×10^{-5}	0.2012
Annealed	−0.261	7.5216×10^{-6}	2.261	−0.296	9.8676×10^{-5}	0.1863
Normalized	−0.267	6.9624×10^{-6}	2.612	−0.293	8.1264×10^{-5}	0.1780
Quenched	−0.278	6.2246×10^{-6}	3.252	−0.301	6.8869×10^{-5}	0.2427
Quenched + aged	−0.262	6.3298×10^{-6}	2.674	−0.286	4.8740×10^{-5}	0.3799

Table 5 Results of CE-corrosion synergy in 3.5 wt.% NaCl solution for different NABs

Sample	Mass loss rate/(mg·cm^{-2}·h^{-1})					
	T	E	C	ΔE	ΔC	S
As-cast	0.9917	0.7332	0.0081	0.1448	0.1056	0.2504
Annealed	1.0583	0.8083	0.0087	0.1363	0.1050	0.2413
Normalized	0.8583	0.6250	0.0080	0.1397	0.0856	0.2253
Quenched	0.5917	0.2167	0.0072	0.2956	0.0722	0.3678
Quenched + aged	0.4917	0.1667	0.0073	0.2688	0.0489	0.3177

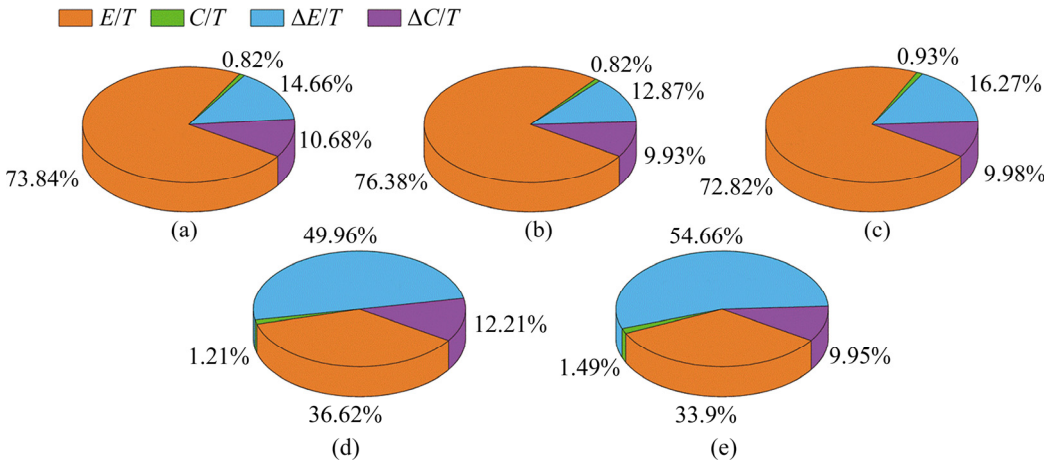

Fig. 13 Contribution of different components to cumulative CE mass loss for different NABs in 3.5 wt.% NaCl solution: (a) As-cast; (b) Annealed; (c) Normalized; (d) Quenched; (e) Quenched + aged

causes the CE mass loss. The $\Delta C/T$ is much smaller than the $\Delta E/T$, indicating that the corrosion-enhanced-CE contributes largely to the CE-corrosion synergy. For the two NABs, the corrosion damage at β' decreases the surface mechanical properties and results in large ΔE. The eroded surface is relatively even with shallow cavities and short cracks because of the high mechanical property (hardness). Therefore, the CE-enhanced-corrosion is not considerable as the corrosion-enhanced-CE.

The corrosion and CE test results indicate that the decrease of the eutectoid microstructure is beneficial to the corrosion resistance improvement of NAB. Both high corrosion resistance and mechanical properties are crucial to ensure the CE resistance of NAB in seawater environments.

4 Conclusions

(1) After annealing, β' transformed into the eutectoid $\alpha+\kappa_{III}$, and more κ_{IV} precipitated from the α matrix. The normalized NAB possessed more β' and a small quantity of eutectoid microstructure. The quenched NAB was composed of Widmanstatten α and martensitic β', and the

precipitation of κ was suppressed because of the high cooling rate. After subsequent aging, fine acicular α and κ precipitated from β'.

(2) The gravimetric measurement results indicated that the order of corrosion resistance from high to low is: quenched > quenched + aged > normalized > as-cast > annealed. Severe SPC occurred in the eutectoid microstructure of the as-cast and annealed NABs, and the β' phase of the normalized NAB. The annealed NAB exhibited the lowest corrosion resistance because it had the largest proportion of eutectoid $\alpha+\kappa_{III}$. The quenched and quenched + aged NABs underwent slight corrosion because of their homogeneous microstructure. The electrochemical test results showed that the corrosion product film on the quenched NAB exhibited the highest protectiveness.

(3) The CE resistance order from high to low is: quenched + aged > quenched > normalized > as-cast > annealed. A positive CE-corrosion synergy existed for each NAB. Deep cavities and long cracks appeared on the surfaces of the as-cast, annealed and normalized NABs because of the relatively low hardness and occurrence of SPC. Mechanical attack dominantly gave rise to the CE damage. The quenched and quenched + aged NABs were more slightly and evenly eroded because of the high hardness. The CE-corrosion synergy played a dominant role in CE degradation, and it was primarily created by the corrosion-enhanced-CE.

Acknowledgments

This research was financially supported by the Fundamental Research Funds for the Central Universities of China (Nos. B210203049, B210204005), the Natural Science Foundation of Jiangsu Province, China (No. BK20191161), the Changzhou Sci & Tech Program, China (No. CJ20210154), and the National Natural Science Foundation of China (Nos. 51601058, 51879089).

References

[1] TUTHILL A H. Guidelines for the use of copper alloys in seawater [J]. Materials Performance, 1987, 26: 12−22.

[2] HASAN F, LORIMER G W, EIDLEY N. The morphology, crystallography, and chemistry of phases in as-cast nickel−aluminum bronze [J]. Metallurgical Transactions A, 1982, 13: 1337−1345.

[3] CULPAN E A, ROSE G. Microstructural characterization of cast nickel aluminum bronze [J]. Journal of Materials Science, 1978, 13: 1647−1657.

[4] CULPAN E A, ROSE G. Corrosion behaviour of cast nickel aluminium bronze in sea water [J]. British Corrosion Journal, 1979, 14: 160−166.

[5] QIN Zhen-bo, ZHANG Qi, LUO Qin, WU Zhong, SHEN Bin, LIU Lei, HU Wen-bin. Microstructure design to improve the corrosion and cavitation corrosion resistance of a nickel−aluminum bronze [J]. Corrosion Science, 2018, 139: 255−266.

[6] SONG Qi-ning, XU Nan, TONG Yao, HUANG Chen-ming, SUN Shou-yu, XU Chen-bo, BAO Ye-feng, JIANG Yong-feng, QIAO Yan-xin, ZHU Zhi-yuan, WANG Zheng-bin. Corrosion and cavitation erosion behaviours of cast nickel aluminium bronze in 3.5% NaCl solution with different sulphide concentrations [J]. Acta Metallurgica Sinica (English Letters), 2019, 32: 1470−1482.

[7] KARIMI A, MARTIN J L. Cavitation erosion of materials [J]. International Metals Reviews, 1986, 31: 1−26.

[8] ALHASHEM A, CACERES P G, RIAD W T, SHALABY H M. Cavitation corrosion behavior of cast nickel−aluminum bronze in seawater [J]. Corrosion, 1995, 51: 331−342.

[9] QIAO Yan-xin, TIAN Zhao-hui, CAI Xiang, CHEN Jian, WANG Yu-xin, SONG Qi-ning, LI Hua-bing. Cavitation erosion behaviors of a nickel-free high-nitrogen stainless steel [J]. Tribology Letters, 2018, 67: 1−9.

[10] ZHANG Lian-min, LI Zhuo-xuan, HU Jia-xiu, MA Ai-li, ZHANG Song, DANIEL E F, UMOH A J, HU Hong-xiang, ZHENG Yu-gui. Understanding the roles of deformation-induced martensite of 304 stainless steel in different stages of cavitation erosion [J]. Tribology International, 2021, 155: 106752.

[11] RICHMAN R H, MCNAUGHTON W P. Correlation of cavitation erosion behavior with mechanical properties of metals [J]. Wear, 1990, 140: 63−82.

[12] DING Xiang, CHENG Xu-dong, YU Xiang, LI Chao, YUAN Cheng-qing, DING Zhang-xiong. Structure and cavitation erosion behavior of HVOF sprayed multi-dimensional WC−10Co4Cr coating [J]. Transactions of Nonferrous Metals Society of China, 2018, 28: 487−494.

[13] SONG Qi-ning, ZHENG Yu-gui, JIANG Sheng-li, NI Ding-rui, MA Zong-yi. Comparison of corrosion and cavitation erosion behaviors between the as-cast and friction-stir-processed nickel aluminum bronze [J]. Corrosion, 2013, 69: 1111−1121.

[14] ZHANG Lian-min, MA Ai-li, YU Hong, UMOH A J, ZHENG Yu-gui. Correlation of microstructure with cavitation erosion behaviour of a nickel−aluminum bronze in simulated seawater [J]. Tribology International, 2019, 136: 250−258.

[15] SONG Qi-ning, TONG Yao, XU Nan, SUN Shou-yu, LI Hui-lin, BAO Ye-feng, JIANG Yong-feng, WANG Zheng-bin, QIAO Yan-xin. Synergistic effect between cavitation erosion and corrosion for various copper alloys in sulphide-containing 3.5% NaCl solutions [J]. Wear, 2020, 450/451: 203258.

[16] NI Ding-rui, XUE Peng, WANG Dong, XIAO Bo-lv, MA Zong-yi. Inhomogeneous microstructure and mechanical

properties of friction stir processed NiAl bronze [J]. Materials Science and Engineering A, 2009, 524: 119−128.

[17] QIN Zhen-bo, XIA Da-hai, ZHANG Yi-wen, WU Zhong, LIU Lei, LV Yu-ting, LIU Yi-chun, HU Wen-bin. Microstructure modification and improving corrosion resistance of laser surface quenched nickel–aluminum bronze alloy [J]. Corrosion Science, 2020, 174: 108744.

[18] LUO Qin, QIN Zhen-bo, WU Zhong, SHEN Bin, LIU lei, HU Wen-bin. The corrosion behavior of Ni−Cu gradient layer on the nickel aluminum-bronze (NAB) alloy [J]. Corrosion Science, 2018, 138: 8−19.

[19] TANG C H, CHENG F T, MAN H C. Improvement in cavitation erosion resistance of a copper-based propeller alloy by laser surface melting [J]. Surface and Coatings Technology, 2004, 182: 300−307.

[20] WU Z, CHENG Y F, LIU L, LV W J, HU W B. Effect of heat treatment on microstructure evolution and erosion–corrosion behavior of a nickel–aluminum bronze alloy in chloride solution [J]. Corrosion Science, 2015, 98: 260−270.

[21] ZENG Yan-hua, YANG Fen-fen, CHEN Zong-ning, GUO En-yu, GAO Min-qiang, WANG Xue-jian, KANG Hui-jun, WANG Tong-min. Enhancing mechanical properties and corrosion resistance of nickel−aluminum bronze via hot rolling process [J]. Journal of Materials Science & Technology, 2021, 61: 186−196.

[22] SONG Qi-ning, ZHENG Yu-gui, NI Ding-rui, MA Zong-yi. Characterization of the corrosion product films formed on the as-cast and friction-stir processed Ni–Al bronze in a 3.5 wt.% NaCl solution [J]. Corrosion, 2015, 71: 606−614.

[23] JAHANAFROOZ A, HASAN F, LORIMER G W, RIDLEY N. Microstructural development in complex nickel–aluminium bronzes [J]. Metallurgical Transactions A, 1983, 14: 1951−1956.

[24] KANG Quan-fei, HU Shu-bing, ZENG Si-qi, CHENG Guang-kun. Heat treatment strengthening of nickel−aluminum bronze alloy for marine propeller [J]. The Chinese Journal of Nonferrous Metals, 2018, 28: 107−115. (in Chinese)

[25] CHEN Rui-ping, LIANG Ze-qin, ZHANG Wei-wen, ZHANG Da-tong, LUO Zong-qiang, LI Yuan-yuan. Effect of heat treatment on microstructure and properties of hot-extruded nickel−aluminum bronze [J]. Transactions of Nonferrous Metals Society of China, 2007, 17: 1254−1258.

[26] ASTM G32—10. Standard test for cavitation erosion using vibratory apparatus [S]. 2010.

[27] SCHUSSLER A, EXNER H E. The corrosion of nickel−aluminum bronzes in seawater. 1: Protective layer formation and the passivation mechanism [J]. Corrosion Science, 1993, 34: 1793−1802.

[28] WHARTON J A, BARIK R C, KEAR G, WOOD R J K, STOKES K R, WALSH F C. The corrosion of nickel−aluminium bronze in seawater [J]. Corrosion Science, 2005, 47: 3336−3367.

[29] SONG Qi-ning, ZHENG Yu-gui, NI Ding-rui, MA Zong-yi. Studies of the nobility of phases using scanning Kelvin probe microscopy and its relationship to corrosion behaviour of Ni–Al bronze in chloride media [J]. Corrosion Science, 2015, 92: 95−103.

[30] WANG Zheng-bin, HU Hong-xiang, ZHENG Yu-gui. Synergistic effects of fluoride and chloride on general corrosion behavior of AISI 316 stainless steel and pure titanium in H_2SO_4 solutions [J]. Corrosion Science, 2018, 130: 203−217.

[31] YUAN S J, PEHKONEN S O. Surface characterization and corrosion behavior of 70/30 Cu–Ni alloy in pristine and sulfide-containing simulated seawater [J]. Corrosion Science, 2007, 49: 1276−1304.

[32] QIAO Yan-xin, WANG Xin-yi, YANG Lan-lan, WANG Xiao-jing, CHEN Jian, WANG Zheng-bin, ZHOU Hui-ling, ZOU Jia-sheng, WANG Fu-hui. Effect of aging treatment on microstructure and corrosion behavior of a Fe−18Cr−15Mn−0.66N stainless steel [J]. Journal of Materials Science & Technology, 2022, 107: 197–206.

[33] TANG Yan-bing, SHEN Xin-wang, LIU Zhi-hong, QIAO Yan-xin, YANG Lan-lan, LU Dao-hua, ZHOU Jia-sheng, XU Jing. Corrosion behaviors of selective laser melted Inconel 718 alloy in NaOH solution [J]. Acta Metallurgica Sinca, 2022, 58: 324−333.

[34] JORCIN J B, ORAZEM M E, PÉBÈRE N, TRIBOLLET B. CPE analysis by local electrochemical impedance spectroscopy [J]. Electrochimica Acta, 2016, 51: 1473−1479.

[35] YIN Mo-yang, LI Zhuo, XIAO Zhu, PANG Yong, LI Ya-ping, SHEN Zi-yan. Corrosion behavior of Cu−Al−Mn−Zn−Zr shape memory alloy in NaCl solution [J]. Transactions of Nonferrous Metals Society of China, 2021, 31: 1012−1022.

[36] SABBAGHZADEH B, PARVIZI R, DAVOODI A, MOAYED M H. Corrosion evaluation of multi-pass welded nickel–aluminum bronze alloy in 3.5% sodium chloride solution: A restorative application of gas tungsten arc welding process [J]. Materials & Design, 2014, 58: 346−356.

[37] NEODO S, CARUGO D, WHARTON J A, STOKES K R. Electrochemical behaviour of nickel−aluminium bronze in chloride media: Influence of pH and benzotriazole [J]. Journal of Electroanalytical Chemistry, 2013, 695: 38−46.

[38] WHARTON J A, STOKES K R. The influence of nickel−aluminium bronze microstructure and crevice solution on the initiation of crevice corrosion [J]. Electrochimica Acta, 2008, 53: 2463−2473.

[39] KEAR G, BARKER B D, WALSH F C. Electrochemical corrosion of unalloyed copper in chloride media—A critical review [J]. Corrosion Science, 2004, 46: 109−135.

[40] SONG Qi-ning, TONG Yao, LI Hui-lin, ZHANG Hao-nan, XU Nan, ZHANG Gen-yuan, BAO Ye-feng, LIU Wen, LIU Zhen-guang, QIAO Yan-xin. Corrosion and cavitation erosion resistance enhancement of cast Ni−Al bronze by laser surface melting [J]. Journal of Iron and Steel Research International, 2022, 29: 359−369.

[41] ZHENG Zhi-bin, LONG Jun, WANG Shuai, LI Hui, WANG Juan, ZHENG Kai-hong. Cavitation erosion−corrosion behaviour of Fe−10Cr martensitic steel microalloyed with Zr in 3.5% NaCl solution [J]. Corrosion Science, 2021, 184: 109382.

[42] BASUMATARY J, WOOD R J K. Different methods of measuring synergy between cavitation erosion and corrosion for nickel aluminium bronze in 3.5% NaCl solution [J]. Tribology International, 2017, 147: 1−12.

[43] ZHENG Yu-gui, LUO Su-zhen, KE Wei. Effect of passivity on electrochemical corrosion behavior of alloys during cavitation in aqueous solutions [J]. Wear, 2007, 262: 1308−1314.
[44] KWOK C T, CHENG F T, MAN H C. Synergistic effect of cavitation erosion and corrosion of various engineering alloys in 3.5% NaCl solution [J]. Materials Science and Engineering A, 2000, 290: 145−154.
[45] ZHANG Bei-bei, WANG Jian-zhang, YAN Feng-yuan. Load-dependent tribocorrosion behaviour of nickel−aluminium bronze in artificial seawater [J]. Corrosion Science, 2018, 131: 252−263.
[46] WOOD R J K. Marine wear and tribocorrosion [J]. Wear, 2017, 376/377: 893−910.

镍铝青铜的显微组织与腐蚀和空蚀行为的关联性

宋亓宁[1,2]，李慧琳[1]，张皓男[1]，洪 浩[1]，许 楠[1]，张根元[1]，包晔峰[1]，乔岩欣[3]

1. 河海大学 机电工程学院，常州 213022；2. 河海大学 教育部疏浚技术工程研究中心，常州 213022；
3. 江苏科技大学 材料科学与工程学院，镇江 212003

摘 要：对铸态镍铝青铜进行 4 种热处理，并对铸态和热处理后的镍铝青铜在 3.5%NaCl(质量分数)溶液中的显微组织、腐蚀和空蚀行为进行对比研究。结果表明，经退火后，铸态中的 β'相转变为共析组织，更多的 κ_{IV} 相从 α 相中析出。正火态镍铝青铜中共析组织含量减少，β'相含量增加，淬火态主要包含 α 和 β'相。在随后的时效过程中，β'相内析出细小的针状 α 和 κ 相。退火态耐腐蚀性最差，这是由于其具有最高含量的共析组织，而共析组织会遭受严重的选择相腐蚀。淬火态表面形成的腐蚀产物膜保护性最好，耐腐蚀性最高。对于铸态、退火和正火态，力学冲击作用是导致空蚀破坏的主导因素。淬火和淬火+时效态合金由于具有较高的硬度，因此耐空蚀性能较好，空蚀−腐蚀交互作用是导致空蚀破坏的主导因素，且腐蚀促进空蚀在交互作用中占比较大。

关键词：热处理；镍铝青铜；腐蚀；空蚀；交互作用

(Edited by Wei-ping CHEN)